Viscosity of MgSiO3 Liquid at Earth's Mantle Conditions: Implications for an Early Magma Ocean

Bijaya B. Karki, *et al.*

Science **328**, 740 (2010);
DOI: 10.1126/science.1188327

27. T. J. Stasevich, C. G. Tao, W. G. Cullen, E. D. Williams, T. L. Einstein, *Phys. Rev. Lett.* **102**, 085501 (2009).
28. P. J. Rous, *Phys. Rev. B* **59**, 7719 (1999).
29. Y. N. Mo, W. G. Zhu, E. Kaxiras, Z. Y. Zhang, *Phys. Rev. Lett.* **101**, 216101 (2008).
30. J. Y. Park *et al.*, *Phys. Rev. Lett.* **95**, 136802 (2005).
31. A. Sperl *et al.*, *Phys. Rev. B* **77**, 085422 (2008).
32. R. S. Sorbello, *Solid State Phys.* **51**, 159 (1997).
33. J. Taylor, H. Guo, J. Wang, *Phys. Rev. B* **63**, 245407 (2001).
34. B. G. Briner, R. M. Feenstra, T. P. Chin, J. M. Woodall, *Phys. Rev. B* **54**, R5283 (1996).
35. J. Homoth *et al.*, *Nano Lett.* **9**, 1588 (2009).
36. Y. Zhang, W. van Drongelen, B. He, T. Block, C. Tegenkamp, *Appl. Phys. Lett.* **89**, 223903 (2006).
37. C. Jin, K. Suenaga, S. Iijima, *Nano Lett.* **8**, 1127 (2008).
38. T. Sun *et al.*, *Phys. Rev. B* **79**, 041402 (2009).
39. M. Rusanen, P. Kuhn, J. Krug, *Phys. Rev. B* **74**, 245423 (2006).
40. D. Dundas, E. J. McEniry, T. N. Todorov, *Nat. Nanotechnol.* **4**, 99 (2009).
41. This work has been supported by the University of Maryland NSF Materials Research Science and Engineering Center under grant DMR 05-20471, including use of the Shared Experimental Facilities. Infrastructure support is also provided by the University of Maryland NanoCenter and the Center for Nanophysics and Advanced Materials.

Supporting Online Material
www.sciencemag.org/cgi/content/full/328/5979/736/DC1
Materials and Methods
Figs. S1 to S4
References
Movie S1

4 January 2010; accepted 7 April 2010
10.1126/science.1186648

Viscosity of $MgSiO_3$ Liquid at Earth's Mantle Conditions: Implications for an Early Magma Ocean

Bijaya B. Karki[1]* and Lars P. Stixrude[2]

Understanding the chemical and thermal evolution of Earth requires knowledge of transport properties of silicate melts at high pressure and high temperature. Here, first-principles molecular dynamics simulations show that the viscosity of $MgSiO_3$ liquid varies by two orders of magnitude over the mantle pressure regime. Addition of water systematically lowers the viscosity, consistent with enhanced structural depolymerization. The combined effects of pressure and temperature along model geotherms lead to a 10-fold increase in viscosity with depth from the surface to the base of the mantle. Based on these calculations, efficient heat flux from a deep magma ocean may have exceeded the incoming solar flux early in Earth's history.

Silicate liquids likely played a crucial role in terrestrial mass and heat transport in Earth's history. Molten silicates would have controlled the dynamics of the predicted magma ocean [a largely or completely molten mantle that is expected during Earth's earliest stages (*1*)] and continue to influence the transport of modern magmas at the present. If such a magma ocean existed, the rates of initial thermal evolution (via convection) and chemical evolution (via crystal settling and melt percolation) of Earth's interior would be primarily controlled by the melt viscosity (*2*). The ability of melts to carry xenoliths from great depths in the mantle (*3*) also depends on the melt viscosity, in addition to melt composition. Moreover, melts are considered to be responsible for the ultralow velocity zone (ULVZ) in the deep mantle detected by seismology (*4*, *5*).

Despite their importance, transport properties, including the viscosity of molten silicates, are unknown over almost the entire mantle pressure regime, which reaches 136 GPa at the core-mantle boundary. Because of experimental difficulties, the viscosity of $MgSiO_3$ liquid, the dominant composition of Earth's mantle, has only been measured at ambient pressures (*6*). In fact, viscosity measurements of any silicate melts have been limited to relatively low pressures (<13 GPa) (*7*–*12*). In many silicate liquids, the viscosity depends non-monotonically on pressure over the range that has been measured, making extrapolations highly uncertain. Theoretical computations serve as a complementary approach. Previous calculations were primarily based on atomistic models (*13*–*15*), which permit much faster computation but have the disadvantage of being based on empirical force fields, the forms of which are uncertain. On the other hand, the first-principles approach is more robust because it makes no assumptions about the nature of bonding or the shape of the charge density and is thus in principle equally applicable to the study of a wide variety of materials problems, including liquids. We previously calculated the structure and thermodynamic properties of $MgSiO_3$ and $MgSiO_3$-H_2O liquids from first principles (*16*, *17*), finding good agreement with extant experimental data over the entire mantle pressure-temperature regime. Unlike these equilibrium properties, the transport properties such as viscosity require much longer simulation (*18*).

Here, we determine the viscosity of two key liquids over the entire mantle pressure regime from density functional theory (*18*). $MgSiO_3$ serves as an analog composition for a magma ocean, whereas $MgSiO_3$-H_2O liquid allows us to explore the role of melt composition, focusing on H_2O as the component that is known to have the largest influence on the viscosity at low pressure (*19*). The shear viscosity (η) was calculated by using the Green-Kubo relation

$$\eta = \frac{V}{3k_B T}\int_0 \left\langle \sum_{i<j} \sigma_{ij}(t+t_0).\sigma_{ij}(t_0) \right\rangle dt \quad (1)$$

where σ_{ij} (i and $j = x, y, z$) is the stress tensor, which is computed directly at every time step of the simulation, V is volume, k_B is the Boltzmann constant, T is temperature, t is time, and t_0 represents the time origin. The shear-stress autocorrelation function (the integrand of Eq. 1) decays to zero more slowly at lower temperature and higher pressure, requiring longer simulation

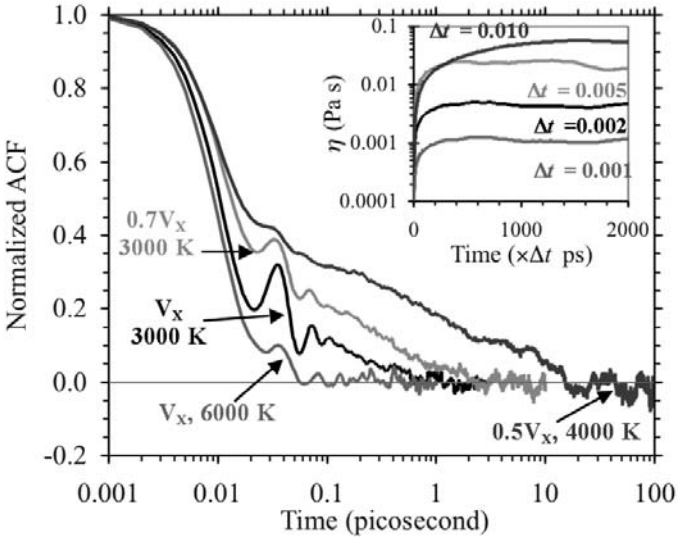

Fig. 1. Time convergences of the calculated stress autocorrelation function (ACF) and viscosity (**inset**) of $MgSiO_3$ melt (without water) at different conditions. The run durations are 18 ps (V_X, 6000 K, 7.5 GPa), 60 ps (V_X, 3000 K, 1.8 GPa), 72 ps ($0.7V_X$, 3000 K, 25 GPa), and 172 ps ($0.5V_X$, 4000 K, 135 GPa), where V_X is the reference volume (38.9 cm^3mol^{-1}).

[1]Department of Computer Science, Department of Geology and Geophysics, Louisiana State University, Baton Rouge, LA 70803, USA. [2]Department of Earth Sciences, University College London, London WC1E 6BT, UK.

*To whom correspondence should be addressed. E-mail: karki@csc.lsu.edu

runs (Fig. 1). We find that the integral values, and hence the computed viscosity, converge over time intervals much shorter than the total simulation durations (Fig. 1, inset). The fact that the shear stress autocorrelation function decays to zero within the time scale of our simulations means that the Maxwell relaxation time of silicate liquids (*20*) remains much shorter than seismic periods over the entire mantle regime and that seismic wave propagation through melts that may exist in the ULVZ will occur in the relaxed limit. We further confirm that the simulated system is in the liquid state at each pressure-temperature condition by examining the mean-square displacements (fig. S1) and radial distribution functions (fig. S2). Our approach is expected to be more robust than the commonly used indirect approach of estimating the melt viscosity from the self-diffusion coefficient via the classic Erying relation (*20*, *21*). The validity of the Eyring relation as applied to silicate liquids has been questioned on the basis of experiments (*11*).

Over most of the pressure range of our investigation, viscosity increases with increasing pressure (Fig. 2A). The calculated viscosity increases by a factor of ~140 for anhydrous silicate melt over the entire mantle pressure regime at 4000 K. The activation volume $V_\eta^* = (d\ln\eta/dP)_T$ varies systematically over most of this range, tending to decrease with increasing pressure and with increasing temperature. At the lowest temperature and pressure, we find that the viscosity behaves anomalously: decreasing with increasing pressure initially, reaching a minimum value near 5 GPa at 3000 K, and then increasing on further compression. Low-pressure experimental studies have found viscosity decreasing with increasing pressure in highly polymerized silicate melts (*8*, *11*, *23*). We attribute the initial decrease in viscosity with increasing pressure to the presence of fivefold coordinated silicon, which acts as a transition state accommodating viscous flow (*16*, *24*). The variation of viscosity in this anomalous regime is small compared with the total variation in viscosity over the mantle pressure-temperature range. The calculated viscosities show large and systematic deviations from Arrhenian behavior (Fig. 2B). The activation energy decreases with increasing temperature, consistent with the behavior of moderately fragile liquids (*25*).

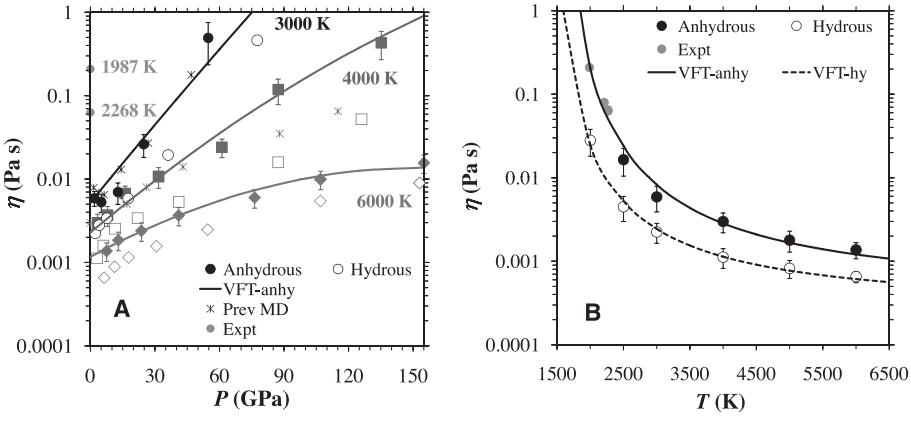

Fig. 2. Calculated viscosity (η) of anhydrous (anhy, solid symbols) and hydrous (hy, open symbols) $MgSiO_3$ melts. Our results are compared with experimental (Expt) data (*6*) at lower temperatures and ambient pressure for anhydrous $MgSiO_3$ liquid. Error bars indicate the statistical uncertainties. (**A**) Pressure variations along 3000 K (circles), 4000 K (squares), and 6000 K (diamonds) isotherms. The anhydrous results can be represented by the modified VFT (Vogel-Fulcher-Tammann) equation (*35*): $\eta(P,T) = \exp[-7.75 + 0.005\,P - 0.00015\,P^2 + (5000 + 135\,P + 0.23P^2)/(T - T_0)]$, with T_0 = 1000 K. Also shown are the results at 3000 K (*14*) and 4000 K (*15*) from previous molecular dynamics (MD) studies of anhydrous liquid based on semi-empirical pair potentials. (**B**) Temperature variations at the reference volume (V_X) together with experimental data (*6*) represented by the VFT equation, $\eta(T) = A\,\exp[\,B/(T - 1000)]$, where A = 0.00033 Pa s and B = 6400 K for anhydrous liquid and A = 0.00024 Pa s and B = 4600 K for hydrous liquid.

Silicate melt with 10 weight percent H_2O is two to four times less viscous than the anhydrous melt at all pressure-temperature conditions studied (Fig. 2). We have previously shown that the self-diffusion coefficients of the hydrous liquid are systematically higher than those of the anhydrous liquid (*26*). The region of anomalous pressure dependence of the viscosity and diffusion are weak or absent in the case of hydrous silicate liquid. Our first-principles results confirm that the dynamical enhancement (smaller viscosity and larger diffusivity) occurs in hydrous silicate liquid because water systematically depolymerizes the melt structure (*27*). The mean O-Si and Si-Si coordination numbers decrease in the presence of water: The hydrous values vary from 1.1 to 1.7 on compression (compared with anhydrous value of 1.4 to 2) and 1.8 to 4.7 (compared with anhydrous value of 2.5 to 5.5), respectively, over the compression range studied (*17*, *26*).

The viscosity of silicate melts increases modestly along temperature profiles characteristic of Earth's interior because of the competing effects of pressure and temperature (Fig. 3). For example, along a slightly super-liquidus magma ocean isentrope (*28*), the viscosity of anhydrous melt increases by a factor of 10 from the surface to the core-mantle boundary. The variations are similar in size but non-monotonic along the estimated mantle solidus and liquidus (*28*). The non-monotonic variation of the viscosity along these curves is due to the rapid increase in temperature with increasing pressure at low pressure. The viscosity profiles of the hydrous melt show similar variations but are systematically shifted downward (Fig. 3).

Our results provide a fundamental basis for any dynamical model of magma ocean evolution. To illustrate, we use our viscosity results and those of previous ab initio simulations of silicate melts to estimate critical dynamical parameters. For a completely molten mantle such as one that may have occurred early in Earth's history (*1*), the estimated Rayleigh and Prandtl numbers (*29*) are ~6 × 10^{30} and ~60, respectively, for the viscosity value of 0.048(10) Pa s for anhydrous $MgSiO_3$ liquid at mid-mantle condition (70 GPa

Fig. 3. Predicted viscosity for magma ocean based on anhydrous silicate liquid results (using the modified VFT relation shown in Fig. 2) along different temperature profiles (**inset**) from (*28*): magma ocean isentrope, mantle liquidus, mantle solidus, and melting curve of pure $MgSiO_3$ perovskite (dashed line). The hydrous result is shown only along the mantle liquidus (gray line). The symbol represents a viscosity value at mid-mantle condition.

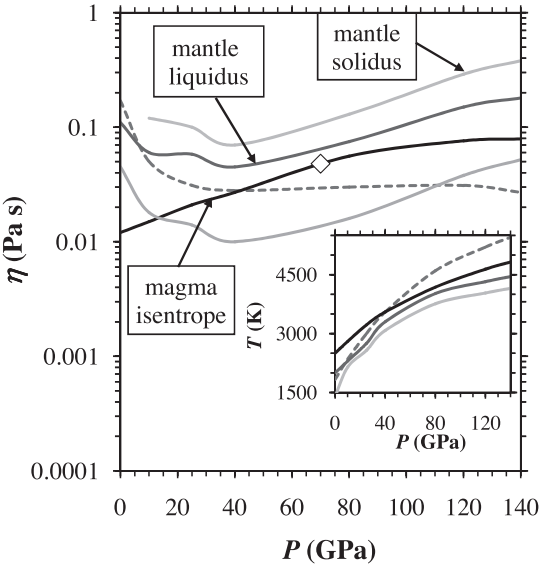

and 4000 K along the magma ocean isentrope, Fig. 3). The Rayleigh number lies in the regime of turbulent convection: The presence of turbulence may substantially influence the settling of crystals as they form upon cooling. The surface heat flux, $F \sim 6 \times 10^4$ W m^{-2}, estimated from mixing length theory far exceeds the incoming solar flux (*30*) and suggests that the surface temperature was set by heat exchange of the magma ocean with a dense silicate atmosphere rather than by solar radiation balance (*2*). This value of F implies a cooling time for the magma ocean ~20 ky (*30*). In fact, a number of processes are likely to increase the cooling time of the magma ocean substantially, including crystallization, which is predicted to initiate in the mid-mantle (*28*) and to separate the magma ocean into upper and basal layers (*31*). The evolution at this stage also depends strongly on the viscosity, which will set the time scale for buoyancy-driven motion of crystals and liquid that can lead to chemical differentiation. The direction of motion will be set by the crystal-liquid density contrast, the sign of which varies with pressure and temperature. Indeed, crystals are expected to float near the base of the mantle (*16*), producing a buoyantly stable basal magma layer that may be long-lived (*31*).

References and Notes

1. R. M. Canup, *Icarus* **168**, 433 (2004).
2. V. S. Solomatov, in *Evolution of the Earth*, D. Stevenson, Ed., vol. 9 of *Treatise on Geophysics*, G. Schubert, Ed. (Elsevier, Amsterdam, 2007), p. 91.
3. S. E. Haggerty, V. Sautter, *Science* **248**, 993 (1990).
4. J. Revenaugh, S. A. Sipkin, *Nature* **369**, 474 (1994).
5. Q. Williams, E. J. Garnero, *Science* **273**, 1528 (1996).
6. G. Urbain, Y. Bottinga, P. Richet, *Geochim. Cosmochim. Acta* **46**, 1061 (1982).
7. I. Kushiro, H. S. Yoder Jr., B. O. Mysen, *J. Geophys. Res.* **81**, 6351 (1976).
8. Y. Bottinga, P. Richet, *Geochim. Cosmochim. Acta* **59**, 2725 (1995).
9. J. E. Reid *et al.*, *Phys. Earth Planet. Inter.* **139**, 45 (2003).
10. H. Behrens, F. Schulze, *Am. Mineral.* **88**, 1351 (2003).
11. D. Tinker *et al.*, *Am. Mineral.* **89**, 1701 (2004).
12. C. Liebske *et al.*, *Earth Planet. Sci. Lett.* **240**, 589 (2005).
13. E. A. Wasserman, D. A. Yuen, J. R. Rustad, *Earth Planet. Sci. Lett.* **114**, 373 (1993).
14. D. J. Lacks, D. Rear, J. A. Van Orman, *Geochim. Cosmochim. Acta* **71**, 1312 (2007).
15. D. Nevins, F. J. Spera, M. S. Ghiorso, *Am. Mineral.* **94**, 975 (2009).
16. L. Stixrude, B. B. Karki, *Science* **310**, 297 (2005).
17. M. Mookherjee, L. Stixrude, B. B. Karki, *Nature* **452**, 983 (2008).
18. Computations were performed by using the VASP software (*32*) with the local density approximation and ultrasoft pseudopotentials as before (*16*, *17*, *26*). Methods are available as supporting material on *Science* Online.
19. L. A. Lange, *Rev. Mineral.* **30**, 331 (1994).
20. M. L. Rivers, I. S. E. Carmichael, *J. Geophys. Res.* **92**, (B9), 9247 (1987).
21. J. Mungall, *Geochim. Cosmochim. Acta* **66**, 125 (2002).
22. T. K. Wan, T. S. Duffy, S. Scandolo, R. Car, *J. Geophys. Res.* **112** (B3), 03208 (2007).
23. G. Giordano, D. B. Dingwell, *Earth Planet. Sci. Lett.* **208**, 337 (2003).
24. C. A. Angell, P. A. Cheeseman, S. Tamaddon, *Science* **218**, 885 (1982).
25. C. A. Angell, *Science* **267**, 1924 (1995).
26. B. B. Karki, D. Bhattarai, M. Mookherjee, L. Stixrude, *Phys. Chem. Miner.* **37**, 103 (2010).
27. E. M. Stolper, *Geochim. Cosmochim. Acta* **46**, 2609 (1982).
28. L. Stixrude, N. de Koker, N. Sun, M. Mookherjee, B. B. Karki, *Earth Planet. Sci. Lett.* **278**, 226 (2009).
29. The Rayleigh and Prandtl numbers are $\mathrm{Ra} = [\alpha\rho g(T_M - T_S)L^3]/(\kappa\eta)$ and $\mathrm{Pr} = \eta/(\rho\kappa)$. We have adopted the density (ρ = 4410 kg m^{-3}) and thermal expansivity ($\alpha = 2.6 \times 10^{-5}$) (*16*) and assumed the depth scale L = 3000 km, acceleration due to gravity g = 10 m s^{-2}, thermal conductivity k = 1.2 W m^{-1} K^{-1} (*33*), thermal diffusivity $\kappa = k/(\rho c_P)$ where the specific heat c_P = 1660 J kg^{-1} K^{-1} (*16*), a mantle potential temperature T_M = 2500 K, the lowest temperature at which the mantle will be completely molten, and a surface temperature T_S = 1000 K set by a dense atmosphere (*2*).
30. The surface heat flux is $F = 0.22k(T_M - T_S)\mathrm{Ra}^{2/7}\mathrm{Pr}^{-1/7}L^{-1}$ (*34*) and the cooling time is $\tau_{cool} = T_M c_P M_M/4\pi R^2 F$, where M_M is the mass of the mantle and R is the radius of Earth.
31. S. Labrosse, J. W. Hernlund, N. Coltice, *Nature* **450**, 866 (2007).
32. G. Kresse, J. Furthmuller, *Comput. Mater. Sci.* **6**, 15 (1996).
33. A. M. Hofmeister, A. G. Whittington, M. Pertermann, *Contrib. Mineral. Petrol.* **158**, 381 (2009).
34. B. I. Shraiman, E. D. Siggia, *Phys. Rev. A* **42**, 3650 (1990).
35. K. R. Harris, L. A. Woolf, M. Kanakubo, *J. Chem. Eng. Data* **50**, 1777 (2005).

36. This work was supported by NSF (EAR-0809489) and the UK National Environmental Research Council (NE/F01787/1). Computing facilities were provided by the Center of Computation and Technology at Louisiana State University. The authors thank J. Brodholt, M. Ghiorso, and S. Karato for useful comments and suggestions.

Supporting Online Material

www.sciencemag.org/cgi/content/full/328/5979/740/DC1
Materials and Methods
Figs. S1 and S2

16 February 2010; accepted 7 April 2010
10.1126/science.1188327

Extreme Deuterium Excesses in Ultracarbonaceous Micrometeorites from Central Antarctic Snow

J. Duprat,[1]* E. Dobrică,[1] C. Engrand,[1] J. Aléon,[1] Y. Marrocchi,[2] S. Mostefaoui,[2] A. Meibom,[2] H. Leroux,[3] J.-N. Rouzaud,[4] M. Gounelle,[2] F. Robert[2]

Primitive interplanetary dust is expected to contain the earliest solar system components, including minerals and organic matter. We have recovered, from central Antarctic snow, ultracarbonaceous micrometeorites whose organic matter contains extreme deuterium (D) excesses (10 to 30 times terrestrial values), extending over hundreds of square micrometers. We identified crystalline minerals embedded in the micrometeorite organic matter, which suggests that this organic matter reservoir could have formed within the solar system itself rather than having direct interstellar heritage. The high D/H ratios, the high organic matter content, and the associated minerals favor an origin from the cold regions of the protoplanetary disk. The masses of the particles range from a few tenths of a microgram to a few micrograms, exceeding by more than an order of magnitude those of the dust fragments from comet 81P/Wild 2 returned by the Stardust mission.

The light element isotopic compositions of undifferentiated interplanetary material provide insights into the physicochemical processes that took place in the coldest regions of the early solar system. Large deuterium excesses are expected in the solid component(s) of comets because their water and HCN molecules exhibit D/H ratios from 2 to 15 times the terrestrial value, respectively (*1*). However, isotopic measurements of fragments of comet 81P/Wild 2 returned by the Stardust mission show moderate D/H ratios that do not exceed three times the terrestrial value, possibly indicating a substantial alteration during impact capture process (*2*). By contrast, large D/H ratios have been observed as micrometer-sized hot spots in organic matter of interplanetary dust particles (IDPs) (*3*, *4*) or primitive meteorites (*5*, *6*). These D excesses may have been inherited from the cold molecular cloud that predated the protosolar nebula (*3*, *5*, *7*) or may be the result of a local process that occurred in the cold outer regions of the protoplanetary disk (*8*, *9*). The nature of the D-rich hot spots and their relationship to the organic matter bulk composition remain a matter of debate (*6*, *10*). Organic matter in meteorites is sparse and disseminated in the matrix, with a maximum bulk concentration on the order of a few weight percent (wt %) (*11*). It is mainly accessible as the acid-insoluble component (IOM) remaining after demineralization of large amounts (grams) of primitive meteorites.

Large numbers of Antarctic micrometeorites (AMMs), which are IDPs with sizes ranging from 20 to 1000 μm, can be recovered from the Antarctic ice cap (*12*). Here, we describe AMMs obtained from the melting and sieving of 3 m^3 of ultraclean snow that fell in the vicinity of the French-Italian CONCORDIA station at Dome C

[1]Centre de Spectrométrie Nucléaire et de Spectrométrie de Masse, Université Paris-Sud 11, CNRS/IN2P3, F-91405 Orsay, France. [2]Laboratoire de Minéralogie et Cosmochimie du Muséum (LMCM), UMR 7202–CNRS INSU, Muséum National d'Histoire Naturelle, 57 Rue Cuvier, 75231 Paris Cedex 05, France. [3]Unité Matériaux et Transformations, Université Lille 1 & CNRS, 59655 Villeneuve d'Ascq, France. [4]Laboratoire de Géologie de l'Ecole Normale Supérieure, UMR CNRS 8538, 24 rue Lhomond, 75231 Paris Cedex 5, France.

*To whom correspondence should be addressed. E-mail: jean.duprat@csnsm.in2p3.fr

In Living Color

Light produced using the chemical process of bioluminescence spans the entire range of the visible spectrum. Bioluminescence has evolved independently several times in the tree of life. However, the majority of bioluminescent organisms reside in the open ocean, where their bioluminescence helps species in over 700 genera evade predators, attract mates, and find food. Widder (p. 704) reviews recent advances in understanding the evolution and distribution of bioluminescence in marine systems.

Kissing Cousins

Neandertals, our closest relatives, ranged across Europe and Southwest Asia before their extinction approximately 30,000 years ago. Green et al. (p. 710) report a draft sequence of the Neandertal genome, created from three individuals, and compare it with genomes of five modern humans. The results suggest that ancient genomes of human relatives can be recovered with acceptably low contamination from modern human DNA. Because ancient DNA can be contaminated with microbial DNA, Burbano et al. (p. 723) developed a target sequence capture approach to obtain 14 kilobases of Neandertal DNA from a fairly poorly preserved sample with a high microbial load. A number of genomic regions and genes were revealed as candidates for positive selection early in modern human history. The genomic data suggest that Neandertals mixed with modern human ancestors some 120,000 years ago, leaving traces of Neandertal DNA in contemporary humans.

Centaurus A Gamma-Ray Emissions

The nearest radio galaxy, Centaurus A, has been studied for many years at all wavelengths. Centaurus A exhibits two lobes of radio emissions that lie either side of the galaxy. The emissions extend over very large distances from the central source, which is thought to be powered by an accreting black hole with a mass around 100 million times that of the Sun. Using the Fermi Large Area Telescope, Abdo et al. (p. 725, published online 1 April) now report the detection of gamma-ray emissions emanating from the radio lobes of Centaurus A. Electrons with energies of 0.1 to 1 teraelectron volts are present in the lobes and are either accelerated in situ or transported efficiently from near the central source. The lobe pressure is comparable to that of the surrounding thermal gas, suggesting that the lobes may be affecting their surroundings.

Patterning a Molecular Glass

Lithographic patterning for device fabrication is usually based on initiating polymerization reactions with photons or electrons in a molecular resist. However, patterning can be achieved by mechanically removing a hard resist with scanning probe microscopy tips, but in many cases the resolution is low and excess material is left on the surface. Pires et al. (p. 732, published online 22 April) found that thin films of organic molecules could form glasses through weak interactions and be patterned to tens of nanometers with a heated scanning probe tip. These patterns could be transferred to other substrates or sculpted into three-dimensional shapes by successive rounds of patterning.

Mixing the Magma Ocean

Molten silicate makes up the majority of the magma we see spewing out of volcanoes, yet the mantle from which these melts originate is largely solid. The high pressures and temperatures at which these melts exist make interrogating their physical properties difficult. Karki and Stixrude (p. 740) used high-powered computational methods to calculate the viscosity profiles of one of the more abundant silicate melt compositions. The addition of water to the melt lowers the viscosity to the point that large mineral grains can sink. Because Earth may have been nearly all liquid in its earliest stages of formation, a deep magma ocean with this viscosity could have controlled the temperature of Earth's early surface.

Dust to Dust

Interplanetary dust particles are thought to sample the most primitive materials in the solar system. Because of their large deuterium enrichments, they are thought to have formed in interstellar molecular clouds—the birthplaces of stars—and to predate the solar system. Duprat et al. (p. 742; see Perspective by Nittler) describe two large interplanetary dust particles collected from Antarctic snow. The particles contain large zones of organic matter with deuterium excesses 10 to 30 times the terrestrial value. Because the organic matter is associated with crystalline silicates similar to those formed within the solar accretion disk, it is expected that the particles themselves formed in the Sun's protoplanetary disk, contradicting the idea that all organics with deuterium excesses are of interstellar origin.

Elementary Steps in Electromigration

Electrical current in small metal wires slowly changes their structure. Features such as surface islands can appear to move against the electron flow for metal ions moving along the terrace, or with it if electrons transfer momentum to neutral ions moving around the edge. Tao et al. (p. 736) present evidence for step-edge diffusion of silver islands, 2 to 50 nanometers in diameter, undergoing electromigration. Forces on the edge atoms at kink sites, where the step changes direction, were unusually large, in part because of the locally higher electron density.

Dangerous Dengue Provocation

One problem with dengue virus is that one infection does not protect against a subsequent infection; secondary infections can result in the severe immunopathology of dengue hemorrhagic fever. Dejnirattisai et al. (p. 745) derived a panel of monoclonal antibodies specific for dengue viruses. These antibodies were mainly

Continued on page 665

CREDITS: (TOP TO BOTTOM) EDITH WIDDER; TAO ET AL.

Published by AAAS

Continued from page 663

directed against the dengue virus precursor membrane protein (prM), and most cross-reacted with all four dengue serotypes. The antibodies were not capable of fully neutralizing the virus, but instead promoted immune responses over a wide range of concentrations. During virus production and virion assembly, maturation of prM is often incomplete, and, consequently, a major part of the host's natural antibody response recognizes a component that is present in variable numbers on the virion. Thus, rather than resulting in complete neutralization, the antibody response promotes virus infection of cells that carry receptors for antibodies.

Tolerating Tumors

Successful tumor growth depends on the ability of the tumor to escape detection by the immune system. Human cancers that express the chemokine receptor CCR7 are associated with tumor metastasis and poor prognosis, suggesting that CCR7-dependent signaling might lead to an immunotolerant tumor microenvironment. **Shields *et al.*** (p. 749; published online 25 March; see the Perspective by **Zindl and Chaplin**) studied a mouse melanoma model in which the tumors expressed varying amounts of the CCR7 ligand, CCL21. Tumors expressing CCL21 exhibited more aggressive growth and attracted a class of suppressive, rather than proinflammatory, leukocytes. Furthermore, the tumor microenvironment was rich in immunosuppressive cytokines and exhibited lymph node–like features. These features were not present in tumors that expressed low amounts of CCL21. Thus, tumor CCL21 expression promotes an immunotolerant tumor microenvironment, which is permissive for tumor growth and spread.

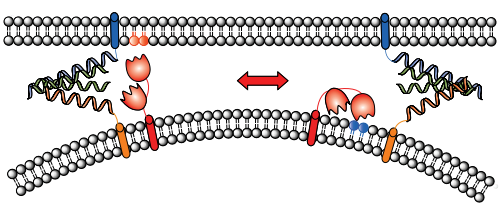

A Trick of the Tail

The synaptic vesicle protein, synaptotagmin 1 (Syt1), acts as the main Ca^{2+}-dependent switch for neurotransmitter release. In vitro studies of the truncated Syt1, which lacks the transmembrane domain, have unveiled the fusion-triggering mechanism of Syt1. However, in vitro approaches using the full-length, membrane-anchored Syt1 have not only failed to recapitulate Ca^{2+}-triggered membrane fusion, but could even inhibit vesicle fusion. In contrast, the membrane anchor is conserved across the Syt family, suggesting a critical functional role for the membrane anchor. Now, using a single vesicle fusion assay, **H.-K. Lee *et al.*** (p. 709) show that the membrane anchor is indeed essential for Syt1 to induce physiological rates of Ca^{2+}-induced vesicle fusion on a 100-millisecond time scale.

Age-Old Problem

With the increase in human life span, there is an associated increase in incidence of age-associated cognitive decline, which causes a huge emotional and economic burden. However, the mechanisms underlying age-associated memory impairment are poorly understood. Now, **Peleg *et al.*** (p. 753; see the Perspective by **Sweatt**) have found that the memory disturbances in the aging mouse brain are associated with specific changes in learning-induced histone acetylation, which interferes with the hippocampal gene-expression program. Restoration of dynamic histone acetylation reinstated cognitive function in the aging mouse.

Target Acquisition

The proper localization of proteins to the correct intracellular destinations is essential for the structure and function of all cells. Most membrane and secretory proteins are targeted to membranes by virtue of a signal sequence that is recognized by signal recognition particle (SRP) as the protein is being translated, forming a complex that docks with target membranes bearing the SRP receptor. Now, **Zhang *et al.*** (p. 757) have found, using cell-free bacterial extracts, that the initial binding of cargo by SRP is not sufficient to discriminate against all the incorrect cargos. Instead, a series of fidelity checkpoints during subsequent steps of the protein-targeting and translocation pathway help reject incorrect cargos.

CREDIT: LEE *ET AL.*